Void growth and coalescence in porous plastic solids

J. Koplik, A. Needleman

VOID GROWTH AND COALESCENCE IN POROUS PLASTIC SOLIDS

J. KOPLIK and A. NEEDLEMAN
Division of Engineering, Brown University, Providence, RI 02912, U.S.A.

Abstract—A boundary value problem simulating a periodic array of spherical voids in an isotropically hardening elastic–viscoplastic matrix is analyzed. The calculations show a shift from a general axisymmetric deformation state to a mode of uniaxial straining at which point the plastic deformation localizes to the ligament between neighboring voids. This event is associated with the accelerated void growth accompanying coalescence. The numerical results are related to the description of void growth and coalescence within a phenomenological constitutive framework for progressively cavitating solids.

1. INTRODUCTION

The nucleation and growth of microvoids plays a central role in the ductile fracture of metals (Puttick, 1959; Rogers, 1960; Beachem, 1963; Gurland and Plateau, 1963). The voids mainly nucleate at second phase particles, either by decohesion of the particle–matrix interface or by particle fracture, and final rupture involves the growth of neighboring voids to coalescence. Based on the approximation of a porous plastic solid by a thick walled spherical shell and carrying out an approximate limit analysis of this configuration, Gurson (1975, 1977) proposed a phenomenological constitutive relation for a progressively cavitating solid. Within this formulation the voids are represented in terms of a single parameter, the void volume fraction. The presence of the voids leads to a macroscopic dilatancy and pressure sensitivity of plastic flow.

Analyses of the influence of microvoids on plastic flow and ductile fracture have been carried out using the constitutive framework introduced by Gurson (1975, 1977). Simple band type localization analyses have given predictions of plastic flow localization at realistic strain levels (Yamamoto, 1978; Needleman and Rice, 1978; Saje *et al.*, 1982). Full finite element analyses have reproduced observed failure behaviors in remarkable detail; exhibiting, for example, the fracture mode transition characteristic of ductile structural metals between a shear fracture in plane strain tension (Tvergaard, 1982a; Becker and Needleman, 1986), and a cup–cone fracture in axisymmetric tension (Tvergaard and Needleman, 1984).

These analyses have actually used modifications to the flow potential originally proposed by Gurson (1975, 1977). The modifications are of two kinds. Based on comparisons of shear band bifurcation predictions obtained from full numerical solutions for arrays of voids and from the Gurson (1975, 1977) constitutive relation, Tvergaard (1981, 1982b) suggested a modification to improve the accuracy of the Gurson (1975, 1977) relation at small void volume fractions. A further modification (Tvergaard and Needleman, 1984) is associated with modelling the complete loss of stress carrying capacity. Although the flow potential proposed by Gurson (1975, 1977) does permit a complete loss of stress carrying capacity at a critical void volume fraction, this critical void volume fraction is unrealistically high.

In this investigation, numerical solutions for the behavior of a cell model of an array of voids are compared with corresponding predictions based on the Gurson (1975, 1977) model and its enhancements. Particular attention is given to the accelerated void growth accompanying final coalescence. Previous cell model analyses have shown the importance of void interaction effects. A doubly periodic array of circular cylindrical voids was analyzed (Needleman, 1972) subject to plane strain tension and estimates of void coalescence strains

were obtained much lower than those based on the isolated void analyses of McClintock (1968) and Rice and Tracey (1969). Subsequent analyses of models of arrays of voids have considered spherical as well as cylindrical void geometries and other deformation histories (Andersson, 1977; Nemat-Nasser and Taya, 1976, 1977; Tvergaard, 1981, 1982b; Becker, 1983; Bourcier *et al.*, 1986). The boundary value problem investigated here is the one previously analyzed by Tvergaard (1982b) and Bourcier *et al.* (1986) that simulates a three-dimensional periodic array of spherical voids. The aggregate is subject to both axial and radial stresses. A circular cylindrical cell surrounding each void is required to remain cylindrical throughout the deformation history in order to simulate the constraint of the surrounding material. By considering histories with different ratios of radial to axial stress the effect of stress triaxiality on void growth is studied. Here, the analyses are actually based on a rate dependent generalization of the original Gurson (1975, 1977) model due to Pan *et al.* (1983), but the focus is on nearly rate independent behavior.

Direct comparisons are made between the numerically obtained stress–strain and void growth response of the cell model and predictions of the modified Gurson (1975, 1977) constitutive relation. Our cell model calculations show a shift in strain state to a mode of uniaxial straining at which point the plastic deformation localizes to the ligament between neighboring voids. This event is associated with the accelerated void growth accompanying coalescence and its modelling in terms of the modification suggested by Tvergaard and Needleman (1984) is discussed.

2. PROBLEM FORMULATION AND NUMERICAL METHOD

The finite element analysis is based on a convected coordinate Lagrangian formulation of the field equations with the initial unstressed state taken as reference. All field quantities are considered to be functions of convected coordinates, y^i, which serve as particle labels, and time t. This formulation has been employed extensively in previous finite element analyses, e.g. Needleman (1972) and Tvergaard (1976), and is reviewed in Needleman (1982).

The position, relative to a fixed Cartesian frame, of a material point in the initial configuration is denoted by $\mathbf{x}$. In the current configuration the material point initially at $\mathbf{x}$ is at $\bar{\mathbf{x}}$. The displacement vector $\mathbf{u}$ and the deformation gradient $\mathbf{F}$ are defined by

$$\mathbf{u} = \bar{\mathbf{x}} - \mathbf{x}, \quad \mathbf{F} = \frac{\partial \bar{\mathbf{x}}}{\partial \mathbf{x}}. \tag{1}$$

Base vectors in the reference configuration (unbarred) and in the current configuration (barred) are given by

$$\mathbf{g}_i = \frac{\partial \mathbf{x}}{\partial y^i}, \quad \bar{\mathbf{g}}_i = \frac{\partial \bar{\mathbf{x}}}{\partial y^i} \tag{2}$$

$$\mathbf{g}^i = g^{ij}\mathbf{g}_j, \quad \bar{\mathbf{g}}^i = \bar{g}^{ij}\bar{\mathbf{g}}_j \tag{3}$$

where g^{ij} and $\bar{g}^{ij}$ are, respectively, the inverses of the metric tensors $g_{ij} = \mathbf{g}_i \cdot \mathbf{g}_j$ and $\bar{g}_{ij} = \bar{\mathbf{g}}_i \cdot \bar{\mathbf{g}}_j$. Attention is confined to quasi-static deformations and, with body forces neglected, the principle of virtual work is written as

$$\int_V \tau^{ij} \delta E_{ij} \, \mathrm{d}V = \int_S T^i \delta u_i \, \mathrm{d}S. \tag{4}$$

Here, τ^{ij} are the contravariant components of Kirchhoff stress ($\boldsymbol{\tau} = J\boldsymbol{\sigma}$, with $\boldsymbol{\sigma}$ the Cauchy stress) on the deformed convected coordinate net and V and S are the volume and surface, respectively, of the body in the reference configuration. The nominal traction components, T^i, and Lagrangian strain components, E_{ij}, are given by

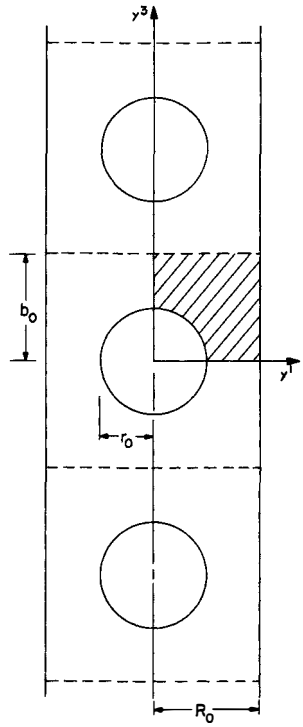

Fig. 1. Axisymmetric model of a material containing an array of spherical voids. Due to the assumed symmetry only the shaded quadrant is analyzed numerically.

$$T^i = (\tau^{ij} + \tau^{kj} u^i_{,k}) v_j \tag{5}$$

$$E_{ij} = \frac{1}{2}(u_{i,j} + u_{j,i} + u^k_{,i} u_{k,j}) \tag{6}$$

where $\boldsymbol{v}$ is the surface normal in the reference configuration, u_j the components of the displacement vector on base vectors in the reference configuration, and $(\ )_{,i}$ denotes covariant differentiation in the reference frame.

The rate boundary value problem is formulated by expanding the principle of virtual work, eqn (4), about the current state to obtain

$$\Delta t \int_V [\dot{\tau}^{ij} \delta E_{ij} + \tau^{ij} \dot{u}^k_{,i} \delta u_{k,j}] \, \mathrm{d}V = \Delta t \int_S T^i \delta u_i \, \mathrm{d}S - \left[\int_V \tau^{ij} \delta E_{ij} \, \mathrm{d}V - \int_S T^i \delta u_i \, \mathrm{d}S \right] \tag{7}$$

where $\dot{(\ )} = \partial(\ )/\partial t$ at fixed y^i and the second term on the right-hand side represents an equilibrium correction term that is used in the numerical procedure to reduce drift from the equilibrium path due to the discrete time step.

A cylindrical coordinate system is used for the specific boundary value problem considered here and we denote the radial coordinate as y^1, the circumferential angle as y^2, and the axial coordinate as y^3. As shown in Fig. 1, we consider spherical voids of radius r_0 located along the axis of a circular cylinder with an initial spacing of $2b_0$ between void centers. The cylinder has initial radius R_0 and attention is confined to axisymmetric deformations so that all field quantities are independent of y^2. Furthermore, the circular cylindrical cell surrounding each particle is required to remain a circular cylinder throughout the deformation history. Within each cell symmetry is assumed about the cell center line so that only the shaded region of Fig. 1 is analyzed numerically. As discussed by Tvergaard (1982b), this axisymmetric configuration can be considered an approximation to a three-dimensional array of hexagonal cylinders.

The boundary conditions for the axisymmetric region analyzed numerically are

$$\dot{u}^3 = 0, \quad \dot{T}^1 = 0, \quad \dot{T}^2 = 0, \quad \text{on } y^3 = 0 \tag{8}$$

$$\dot{T}^i = 0, \quad \text{on } (y^1)^2 + (y^3)^2 = r_0^2 \tag{9}$$

$$\dot{u}^3 = \dot{U}_3 = \dot{\varepsilon}_\infty b, \quad \dot{T}^1 = 0, \quad \dot{T}^2 = 0, \quad \text{on } y^3 = b_0 \tag{10}$$

$$\dot{u}^1 = \dot{U}_1, \quad \dot{T}^3 = 0, \quad \dot{T}^2 = 0, \quad \text{on } y^1 = R_0. \tag{11}$$

Here, $\dot{\varepsilon}_\infty$ is a prescribed constant while $\dot{U}_1$ is determined by the analysis. With these boundary conditions, the deformed circular cylindrical cell has radius $R = R_0 + U_1$, and height $2b = 2b_0 + 2U_3$.

The lateral displacement rate, $\dot{U}_1$ is determined from the condition that the average macroscopic true stresses acting on the cell follow the proportional history

$$\frac{\Sigma_1}{\Sigma_3} = \frac{\dot{\Sigma}_1}{\dot{\Sigma}_3} = \rho \tag{12}$$

with ρ a prescribed constant and

$$\Sigma_1 = \frac{R_0 b_0}{Rb}\left\{\frac{1}{b_0}\int_0^{b_0} [T^1]_{y^1 = R_0}\, \mathrm{d}y^3\right\} \tag{13}$$

$$\Sigma_3 = \frac{R_0^2}{R^2}\left\{\frac{2}{R_0^2}\int_0^{R_0} [T^3]_{y^3 = b_0} y^1\, \mathrm{d}y^1\right\}. \tag{14}$$

The material is characterized as an isotropically hardening elastic–viscoplastic solid and the total rate of deformation, $\mathbf{D}$, is written as the sum of an elastic part, $\mathbf{D}^e$, and a plastic part, $\mathbf{D}^p$, with

$$\mathbf{D}^e = \frac{1+\nu}{E}\hat{\boldsymbol{\tau}} - \frac{\nu}{E}(\hat{\boldsymbol{\tau}}:\mathbf{I})\mathbf{I} \tag{15}$$

$$\mathbf{D}^p = \frac{3\dot{\bar{\varepsilon}}}{2\bar{\sigma}}\boldsymbol{\tau}' \tag{16}$$

where $\hat{\boldsymbol{\tau}}$ is the Jaumann rate of Kirchhoff stress, $\mathbf{I}$ the identity tensor, $\hat{\boldsymbol{\tau}}:\mathbf{I}$ the trace of $\hat{\boldsymbol{\tau}}$, $\dot{\bar{\varepsilon}}$ the effective plastic strain rate, E is Young's modulus, ν is Poisson's ratio and

$$\boldsymbol{\tau}' = \boldsymbol{\tau} - \frac{1}{3}(\boldsymbol{\tau}:\mathbf{I})\mathbf{I}, \quad \bar{\sigma}^2 = \frac{3}{2}\boldsymbol{\tau}':\boldsymbol{\tau}' \tag{17}$$

$$\dot{\bar{\varepsilon}} = \dot{\varepsilon}_0[\bar{\sigma}/g(\bar{\varepsilon})]^{1/m}, \quad g(\bar{\varepsilon}) = \sigma_0(\bar{\varepsilon}/\varepsilon_0 + 1)^N, \quad \varepsilon_0 = \sigma_0/E. \tag{18}$$

Here, $\bar{\varepsilon} = \int \dot{\bar{\varepsilon}}\, \mathrm{d}t$ and the function $g(\bar{\varepsilon})$ represents the effective stress vs effective strain response in a tensile test carried out at a strain rate such that $\dot{\bar{\varepsilon}} = \dot{\varepsilon}_0$. Also, σ_0 is a reference strength and N and m are the strain hardening exponent and strain rate hardening exponent, respectively.

Combining eqns (15) and (16) and inverting gives

$$\hat{\boldsymbol{\tau}} = \mathscr{L}:(\mathbf{D} - \mathbf{D}^p). \tag{19}$$

In component form, on the current base vectors, eqn (19) becomes

$$\mathring{\tau}^{ij} = \mathscr{L}^{ijkl}\dot{E}_{kl} - \dot{P}^{ij} \tag{20}$$

where the Lagrangian strain rate components appear through the identity $\dot{E}_{ij} = \bar{\mathbf{g}}_i \cdot \mathbf{D} \cdot \bar{\mathbf{g}}_j$ and

$$\mathscr{L}^{ijkl} = \frac{E}{(1+\nu)}\left[\frac{1}{2}(\bar{g}^{ik}\bar{g}^{jl} + \bar{g}^{il}\bar{g}^{jk}) + \frac{\nu}{(1-2\nu)}\bar{g}^{ij}\bar{g}^{kl}\right] \tag{21}$$

$$\dot{P}^{ij} = \frac{3\dot{\bar{\varepsilon}}}{2\bar{\sigma}}\mathscr{L}^{ijkl}\tau'_{lk}. \tag{22}$$

The covariant components of the Lagrangian strain rate tensor, $\dot{E}_{kl}$, on the reference base vectors, are given by

$$\dot{E}_{ij} = \frac{1}{2}(F^k_{.i}\dot{F}_{kj} + F^k_{.j}\dot{F}_{ki}). \tag{23}$$

For use in eqn (7), eqn (20) is expressed in terms of the contravariant components (on the current base vectors) of the convected rate of Kirchhoff stress

$$\mathring{\tau}^{ij} = C^{ijkl}\dot{E}_{kl} - \dot{P}^{ij} \tag{24}$$

where

$$C^{ijkl} = \mathscr{L}^{ijkl} - \frac{1}{2}[\bar{g}^{ik}\tau^{jl} + \bar{g}^{il}\tau^{jk} + \bar{g}^{jk}\tau^{il} + \bar{g}^{jl}\tau^{ik}]. \tag{25}$$

The deformation history is calculated in a linear incremental manner and, in order to increase the stable time step, the rate tangent modulus method of Peirce *et al.* (1984) is used. This is a forward gradient method based on an estimate of the plastic strain rate in the interval between t and $t+\Delta t$. The incremental boundary value problem is solved using a combined finite element Rayleigh–Ritz method (Tvergaard, 1976).

3. NUMERICAL RESULTS

In this investigation we explore the parameter dependence of void growth in proportional stressing histories using the axisymmetric cell model in Fig. 1. The parameters varied are initial void volume fraction, stress state triaxiality, and matrix material strain hardening. The material properties that remain fixed are given by $E/\sigma_0 = 500$, $\nu = 1/3$ and $m = 0.01$. Three values of the strain hardening exponent, N in eqns (18), are used: $N = 0.2$, 0.1, and 0, where $N = 0$ corresponds to a non-hardening solid.

To define the stress state triaxiality we introduce the macroscopic effective stress, Σ_e, and the macroscopic hydrostatic stress, Σ_h, by

$$\Sigma_e = |\Sigma_3 - \Sigma_1|, \quad \Sigma_h = \frac{1}{3}(\Sigma_3 + 2\Sigma_1) \tag{26}$$

and the triaxiality ratio, T, is then defined as

$$T = \frac{\Sigma_h}{\Sigma_e} = \frac{1}{3}\left[\frac{1+2\rho}{1-\rho}\right] \tag{27}$$

where ρ is the stress proportionality factor in eqn (12).

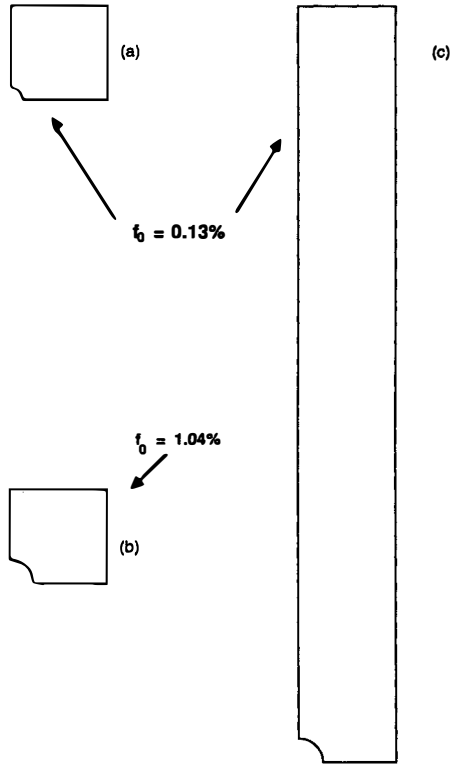

Fig. 2. The three cell geometries analyzed. Only the quadrant analyzed numerically is shown: (a) $b_0/R_0 = 1.0, f_0 = 0.0013$; (b) $b_0/R_0 = 1.0, f_0 = 0.0104$; (c) $b_0/R_0 = 8.0, f_0 = 0.0013$.

The focus here is on triaxiality ratios $1 \leqslant T \leqslant 3$, which cover the range from rather blunt notched bar specimens for which $T \approx 1$ (Needleman and Tvergaard, 1984), to the triaxiality prevailing in crack tip fields for lightly hardening solids, $T \approx 3$ (McMeeking, 1977). In particular, we will present numerical results for $T = 1.0$, 2.0 and 3.0, which correspond to $\rho = 0.40$, 0.625 and 0.73, respectively.

Two initial void volume fractions are considered, $f_0 = 0.0104$ and 0.0013. For a square cell ($b_0/R_0 = 1$, Figs 2(b) and (a)) these correspond to $r_0/R_0 = 0.25$ and 0.125, respectively. We also carry out a few computations with $r_0/R_0 = 0.25$ and $b_0/R_0 = 8.0$ (Fig. 2(c)). This gives an initial void volume fraction of $f_0 = 0.0013$, but with the nearest distance between voids the same as for the square cell with $f_0 = 0.0104$.

A typical finite element mesh used in the square cell computations is shown in Fig. 3. The mesh consists of 480 quadrilateral elements, 24 around the void and 20 in the radial direction. Each quadrilateral consists of four "crossed" linear displacement triangles.

Figure 4 shows the square unit cell model response with $N = 0.1$ and an initial void volume fraction $f_0 = 0.0104$. The macroscopic effective stress–macroscopic effective strain curve in Fig. 4(a) shows the competition between matrix material strain hardening and porosity induced softening. Here, the macroscopic effective stress is given in eqn (26), and the macroscopic effective strain can be conveniently expressed, for the axisymmetric cell, by

$$E_e = \frac{2}{3}|E_3 - E_1| \tag{28}$$

where $E_3 = \ln(b/b_0)$ and $E_1 = \ln(R/R_0)$, with b and R being the current cell height and radius, respectively. As the deformation progresses, a maximum effective stress is reached and, subsequently, a rapid stress drop occurs. The delay between the effective stress maximum and the drop increases with decreasing triaxiality.

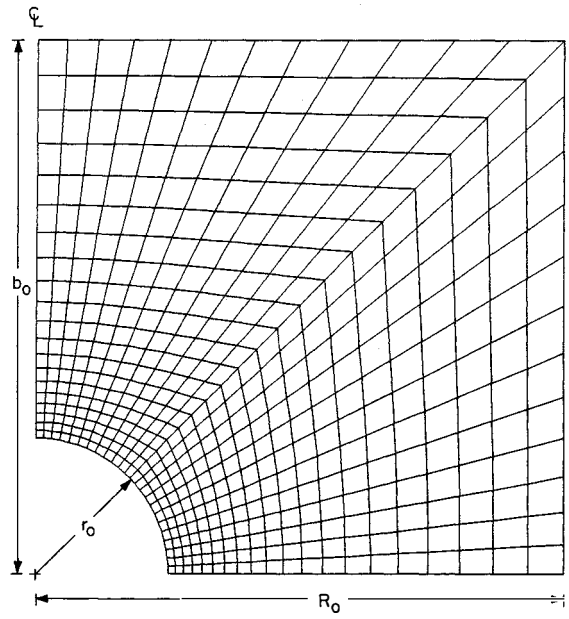

Fig. 3. Finite element mesh used for $b_0/R_0 = 1.0, f_0 = 0.0104$. There are 480 quadrilateral elements, each consisting of four "crossed" linear displacement triangles.

Figure 4(b) shows the evolution of the void volume fraction. The void volume fraction is computed via

$$f = 1 - \frac{V_0}{V}(1-f_0) - \frac{\Delta V_e}{V} \tag{29}$$

where V_0 is the volume of the undeformed cell, f_0 the initial void volume fraction, and ΔV_e the increase in the volume of the cylindrical cell due to the elastic dilation arising from the imposed hydrostatic stress. The elastic dilation in eqn (29) is approximated by

$$\Delta V^e = V_0(1-f_0)\frac{3(1-2\nu)}{E}\Sigma_h. \tag{30}$$

Figure 4(c) illustrates the change in cell radius as a function of effective strain. This last figure shows that an effective strain is eventually reached at which the cell radius remains constant. This implies that further deformation takes place in a uniaxial straining mode which corresponds to flow localization into the ligament between radially adjacent voids. As can be seen in Fig. 4(b), the void volume fraction increases rapidly at this point and this event is associated with the load drop in Fig. 4(a). The computations are terminated when $f = 0.08$.

Corresponding results for $f_0 = 0.0013$ are shown in Fig. 5. The response is qualitatively similar to that in Fig. 4, but the effective stress maximum and the uniaxial straining state are achieved at larger macroscopic effective strains. In Fig. 5, where $f_0 = 0.0013$, the shift to a uniaxial macroscopic straining state, to a reasonable approximation, occurs at the same void volume fraction for all three values of stress triaxiality. On the other hand, for the larger of the two void volume fractions considered here, $f_0 = 0.0104$ (Fig. 4), there is a much larger spread in the void volume fraction at which this event takes place. It is difficult, however, to identify precisely the value of the void volume fraction at which the uniaxial straining state is attained. As shown in Figs 4 and 5, the strain associated with this event can readily be found, but the void volume fraction increases rapidly at this point and small differences in identifying the critical strain give large differences in the critical void volume fraction. Even so, such differences in values of critical void volume fraction were

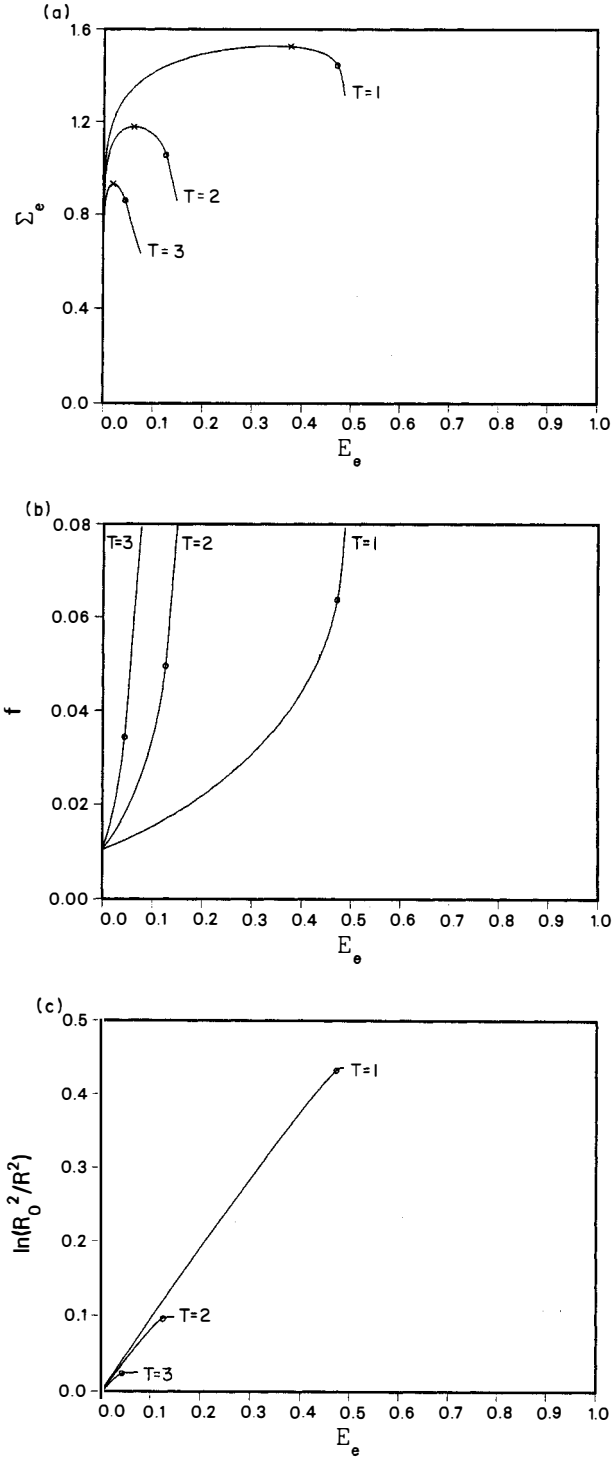

Fig. 4. Finite element results for $b_0/R_0 = 1.0, f_0 = 0.0104$ and $N = 0.1$ with stress triaxialities $T = 1.0$, 2.0, and 3.0. (a) Macroscopic effective stress–effective strain response. The maximum stress points are indicated by ×. (b) Void volume fraction vs macroscopic effective strain. (c) Area strain vs macroscopic effective strain. The shift to a uniaxial straining deformation mode is marked by ○.

observed to be less than ± 0.01 for a reasonable spread of possible critical strains. Results analogous to those in Figs 4 and 5 have been obtained for $N = 0$ and 0.2 and will be discussed in conjunction with a phenomenological constitutive description of porous plastic solids.

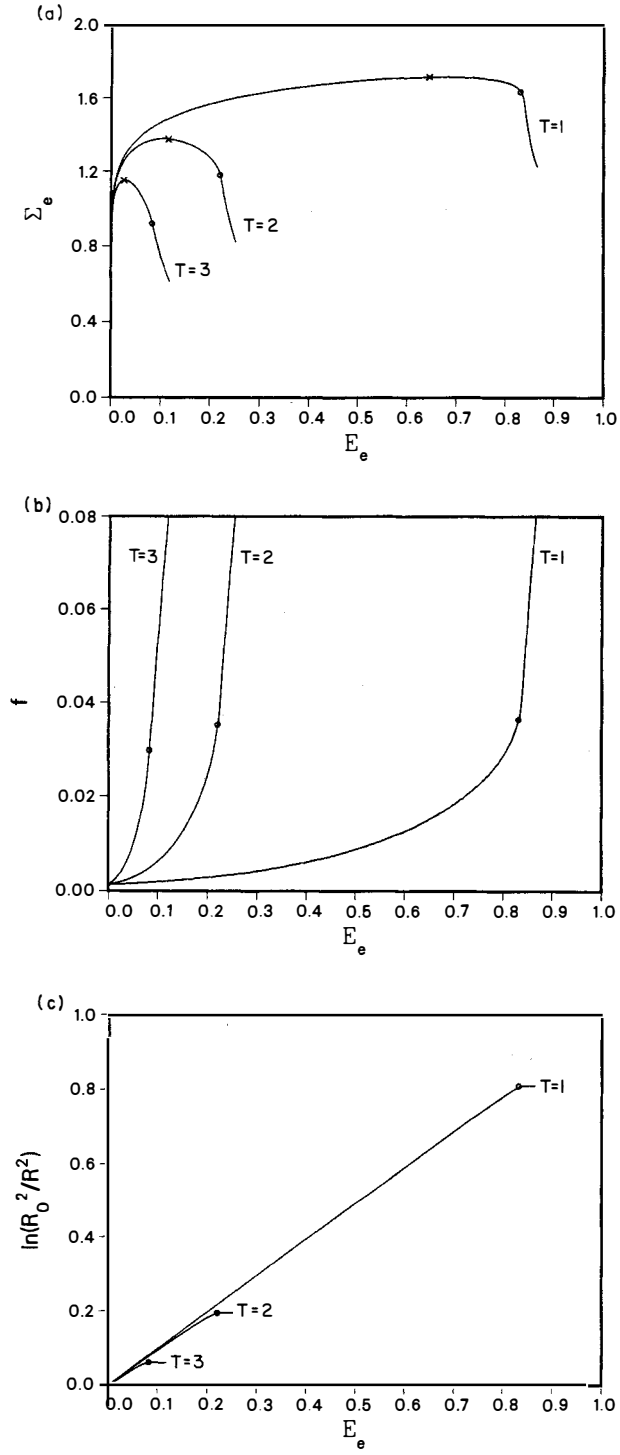

Fig. 5. Finite element results for $b_0/R_0 = 1.0, f_0 = 0.0013$ and $N = 0.1$ with stress triaxialities $T = 1.0$, 2.0, and 3.0. (a) Macroscopic effective stress–effective strain response. The maximum stress points are indicated by $\times$. (b) Void volume fraction vs macroscopic effective strain. (c) Area strain vs macroscopic effective strain. The shift to a uniaxial straining deformation mode is marked by $\bigcirc$.

Figure 6 shows contours of constant plastic strain, $\bar{\varepsilon}$, at various stages of void growth for the case with $T = 2.0$, $f_0 = 0.0104$ and $N = 0.1$. The shift to a macroscopic uniaxial straining state has taken place between Figs 6(c) and (d). Rather large strains develop once the necking down process begins. The finite element mesh becomes highly distorted which

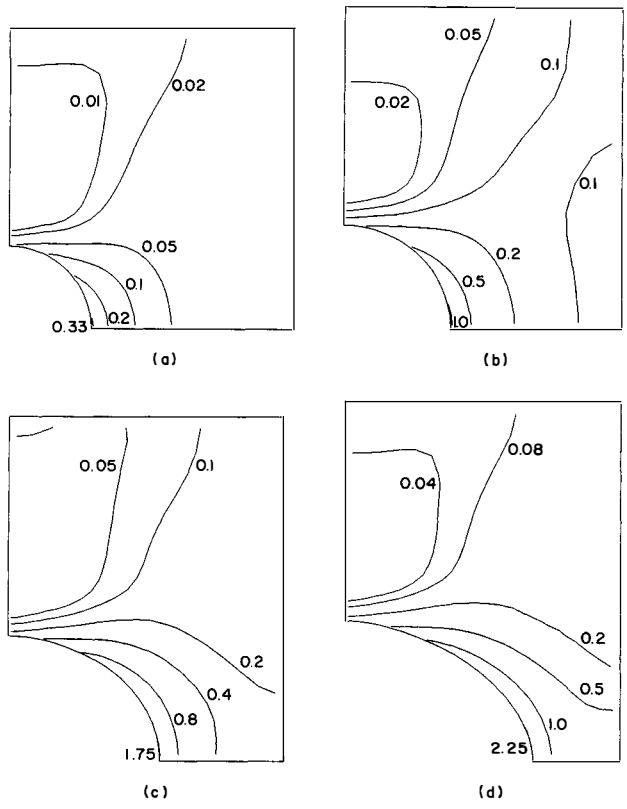

Fig. 6. Contours of constant plastic strain, $\bar{\varepsilon}$, in the deformed configuration of the quadrant analyzed numerically for the case where $b_0/R_0 = 1.0$, $f_0 = 0.0104$, $N = 0.1$, and $T = 2$: (a) $E_e = 0.0293$; (b) $E_e = 0.0945$; (c) $E_e = 0.146$; (d) $E_e = 0.18$.

gives some mesh induced stiffening. This is responsible for the curvature at the end of the falling portion of the stress–strain curves in Figs 4 and 5 (and in subsequent figures). We also note that, although the maximum strains occur along the void surface at all stages of deformation in Fig. 6, the peak hydrostatic tension moves out to the cell boundary along the y^1-axis, i.e. to the point midway along the ligament between adjacent voids. This occurs when the void evolves into a prolate shape as well as when it takes on the oblate shape in Fig. 6.

The void shape depends on the triaxiality level and deformed meshes for the three triaxiality levels in Fig. 5 are shown in Fig. 7. At $T = 1.0$ ($\rho = 0.40$), the void evolves into a prolate shape, whereas for the higher triaxiality values $T \geqslant 2.0$ ($\rho \geqslant 0.625$), the void becomes oblate. For an isolated spherical void in a rigid–perfectly plastic solid, the transition between a prolate shape and an oblate shape occurs for $T = 1.51$ ($\rho = 0.54$) (Budiansky *et al.*, 1982).

Figure 8 illustrates the effect of cell shape on the stress–strain response with $T = 2.0$. Results are shown for the three cell shapes of Fig. 2. Until the stress drop, the stress–strain response is the same for both calculations with $f_0 = 0.0013$. However, localization sets in at a much lower strain for the cell with $b_0/R_0 = 8.0$ than for the square cell. For the elongated cell, the shift to an overall uniaxial straining state occurs when $f \approx 0.003$ as compared with $f \approx 0.03$ for the square cell. The void spacing at which the shift to a uniaxial straining state occurs was also computed. Define r_1 as the distance from the origin to the void surface along the y^1-axis and r_3 as the distance from the origin to the void surface along the y^3-axis. The ligament between voids is then $2(R-r_1)$, where R is the current cell radius, and the void length along the tensile axis is $2r_3$. For $f_0 = 0.0013$, the shift to a uniaxial straining state occurs at $r_3/(R-r_1) = 0.28$ with $b_0/R_0 = 1.0$, while with $b_0/R_0 = 8.0$, $r_3/(R-r_1) = 0.49$. We note that for both $b_0/R_0 = 1.0$ and 8.0 the void evolves into an oblate shape with $r_1/r_3 \approx 1.1$ (Fig. 7(b)). For the case with $f_0 = 0.0104$, $r_3/(R-r_1) = 0.49$ at the shift to a uniaxial straining state (the void shape is more nearly spherical in this case with

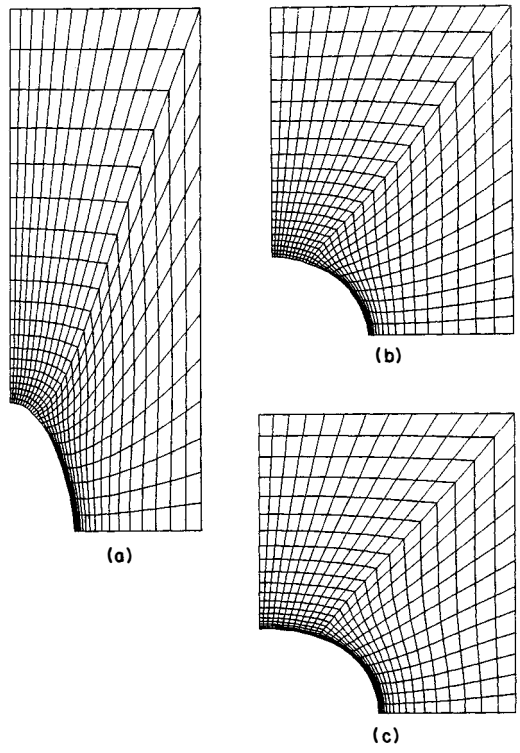

Fig. 7. Deformed meshes for the case where $b_0/R_0 = 1.0$, $f_0 = 0.0013$ and $N = 0.1$ illustrating the effect of stress triaxiality on deformed void shape. The initial cell shape is shown in Fig. 2(a): (a) $T = 1.0$, $E_e = 0.668$, $f = 0.0163$; (b) $T = 2.0$, $E_e = 0.200$, $f = 0.024$; (c) $T = 3.0$, $E_e = 0.0916$, $f = 0.042$.

$r_1/r_3 \approx 1.03$). Hence, in Fig. 8 the initial stress–strain response is primarily a function of void volume fraction, while the onset of localization primarily depends on spacing.

The value of $r_3/(R-r_1)$ at the shift to a uniaxial straining state depends on triaxiality as shown by calculations with $T = 1.0$. With $f_0 = 0.0013$, $b_0/R_0 = 1.0$ and 8.0 give $r_3/(R-r_1) = 1.06$ and 1.08, respectively, at the onset of strain localization onto the ligament between adjacent voids. At this lower triaxiality the void takes on a prolate shape, as in Fig. 7(a); at the shift to a uniaxial straining state $r_3/r_1 = 2.0$ with $b_0/R_0 = 1.0$ and $r_3/r_1 = 1.4$ with $b_0/R_0 = 8.0$. Brown and Embury (1973) have proposed a void coalescence criterion based on the void length parallel to the tensile axis being equal to the void spacing. At the lower stress triaxiality, $T = 1.0$, the Brown and Embury (1973) spacing criterion provides a good approximation in the two cases considered here, with the spacing identified with the

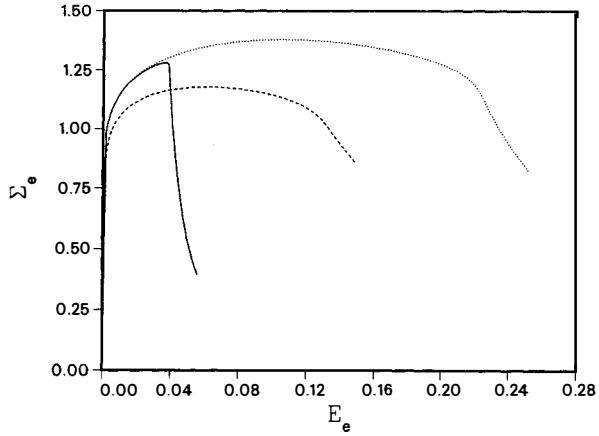

Fig. 8. Macroscopic effective stress–strain curves for $N = 0.1$, $T = 2.0$: $b_0/R_0 = 8.0$, $f_0 = 0.0013$ (——); $b_0/R_0 = 1.0$, $f_0 = 0.0013$ (···); $b_0/R_0 = 1.0$, $f_0 = 0.0104$ (– – –).

ligament length $2(R-r_1)$. With $T = 2.0$ the shift to a uniaxial straining state occurs before this condition is satisfied.

4. PHENOMENOLOGICAL DESCRIPTION OF VOID GROWTH

The cell model calculations will be related to a rate sensitive version of the Gurson (1975, 1977) constitutive relation (Pan *et al.*, 1983). Within the Gurson (1975, 1977) constitutive framework, the porosity is characterized by a single scalar internal variable f, the void volume fraction. For the fully dense material, $f = 0$, the isotropic hardening viscoplastic solid used in the cell model calculations is recovered. The flow potential introduced by Gurson (1975, 1977) has the form

$$\Phi = \frac{\sigma_e^2}{\bar{\sigma}^2} + 2q_1 f^* \cosh\left(\frac{3q_2\sigma_h}{2\bar{\sigma}}\right) - 1 - q_1^2 f^{*2} = 0. \tag{31}$$

Here σ_e is the Mises effective stress, $\sigma_h = \frac{1}{3}\boldsymbol{\sigma}:\mathbf{I}$ the hydrostatic stress, and $\bar{\sigma}$ the average strength of the matrix material. Parameters q_1 and q_2 were introduced by Tvergaard (1981, 1982b) to bring shear band bifurcation predictions of the Gurson (1975, 1977) constitutive relation into closer agreement with corresponding results of full numerical analyses of a periodic array of voids.

Function f^* was proposed by Tvergaard and Needleman (1984) to account for the effects of rapid void coalescence at failure. Initially $f^* = f$, as originally proposed by Gurson (1975, 1977) but at some critical void fraction, f_c, the dependence of f^* on f is increased in order to simulate a more rapid decrease in strength as the voids coalesce

$$f^* = \begin{cases} f, & f \leqslant f_c \\ f_c + \dfrac{f_u^* - f_c}{f_f - f_c}(f - f_c), & f > f_c. \end{cases} \tag{32}$$

The constant f_u^* is the value of f^* at zero stress in eqn (31), i.e. $f_u^* = 1/q_1$. As $f \to f_f$, $f^* \to f_u^*$ and the material loses all stress carrying capacity. Based on experimental studies discussed by Brown and Embury (1973) and Goods and Brown (1979) and on numerical results by Andersson (1977), Tvergaard and Needleman (1984) suggested that the values of f_c and f_f be taken as 0.15 and 0.25, respectively.

In general, the evolution of the void volume fraction results from the growth of existing voids and the nucleation of new voids. Here, however, attention is confined to void growth only. The rate of increase of void volume fraction due to the growth of existing voids is determined from plastic incompressibility of the matrix material

$$\dot{f} = (1-f)\mathbf{D}^p:\mathbf{I}. \tag{33}$$

The plastic part of the rate of deformation, $\mathbf{D}^p$, is taken in a direction normal to the flow potential and is given by

$$\mathbf{D}^p = \dot{\Lambda}\frac{\partial\Phi}{\partial\boldsymbol{\sigma}}. \tag{34}$$

By setting the plastic work rate equal to the matrix dissipation we obtain

$$\boldsymbol{\sigma}:\mathbf{D}^p = (1-f)\bar{\sigma}\dot{\bar{\varepsilon}}. \tag{35}$$

By combining eqns (34) and (35) the plastic flow proportionality factor, $\dot{\Lambda}$, is determined as

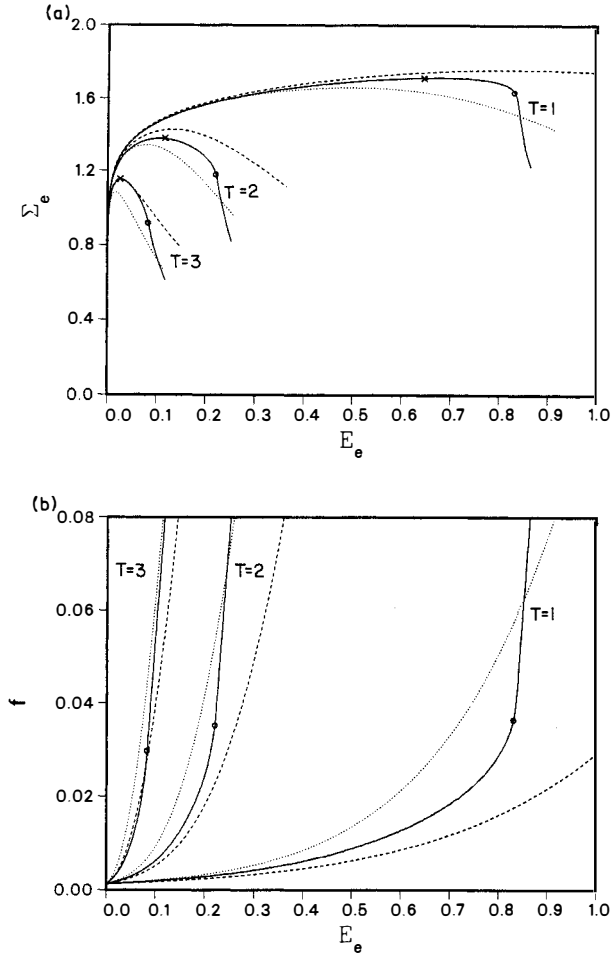

Fig. 9. Comparison of cell model response with the predictions of the modified Gurson (1975, 1977) model with $q_1 = 1.0, q_2 = 1.0$ (– – –) and with $q_1 = 1.5, q_2 = 1.0$ (· · ·). Results are shown for $N = 0.1$, $b_0/R_0 = 1.0, f_0 = 0.0013$, with stress triaxialities, $T = 1.0$, 2.0, and 3.0. (a) Macroscopic effective stress vs macroscopic effective strain. (b) Void volume fraction vs macroscopic effective strain. The cell model response is the solid line and ○ marks the shift to a uniaxial straining deformation mode.

$$\dot{\Lambda} = \frac{(1-f)\bar{\sigma}\dot{\bar{\varepsilon}}}{\boldsymbol{\sigma} : \dfrac{\partial \Phi}{\partial \boldsymbol{\sigma}}}. \tag{36}$$

Writing the rate of deformation tensor as the sum of an elastic part, $\mathbf{D}^e$, and a plastic part, $\mathbf{D}^p$, and then inverting, gives the expression for the Jaumann rate of Cauchy stress, $\hat{\boldsymbol{\sigma}}$, as

$$\hat{\boldsymbol{\sigma}} = \mathscr{L} : (\mathbf{D} - \mathbf{D}^p) \tag{37}$$

where $\mathscr{L}$ is the tensor of (isotropic) linear elastic moduli (21).

The effective stress and hydrostatic stress entering the flow potential, eqn (31), can be identified with the corresponding macroscopic stress quantities, eqns (26), of the cell model. The constitutive equations of the Gurson (1975, 1977) model can readily be solved numerically for various proportional stressing histories and such solutions are compared with cell model predictions in Figs 9–13. In each figure the macroscopic effective stress–effective strain curve and the void volume fraction evolution are compared. In each case the effective strain at which the shift to uniaxial straining takes place is marked.

Figure 9 shows a comparison with the original Gurson (1975, 1977) relation, $q_1 = 1.0$, $q_2 = 1.0$, and Tvergaard's (1981, 1982b) suggested values, $q_1 = 1.5$, $q_2 = 1.0$, for $N = 0.1$ and $f_0 = 0.0013$. Until the shift to a uniaxial straining state the response of the cell model

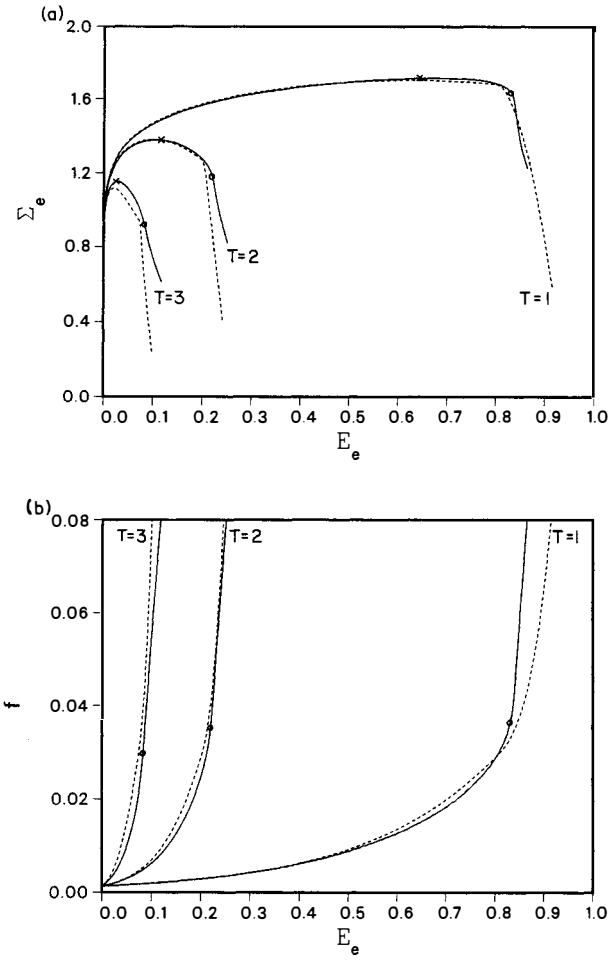

Fig. 10. Comparison of cell model response with the predictions of the modified Gurson (1975, 1977) model using $q_1 = 1.25$, $q_2 = 1.0$ and incorporating the function $f^*(f)$ with $f_c = 0.03$ and $f_f = 0.13$ in eqn (32). As in Fig. 9, results are shown for $N = 0.1$, $b_0/R_0 = 1.0$, $f_0 = 0.0013$, with stress triaxialities, $T = 1.0$, 2.0, and 3.0. (a) Macroscopic effective stress vs macroscopic effective strain. (b) Void volume fraction vs macroscopic effective strain. The cell model response is the solid line and ○ marks the shift to a uniaxial straining deformation mode.

lies between the two sets of phenomenological curves. Subsequently, the void volume fraction increases more rapidly and the stress falls more sharply than either of the Gurson (1975, 1977) relation predictions. It is this sharper stress drop and accompanying increase in void volume fraction growth rate that the function $f^*(f)$ in eqn (32) is intended to model (also see Figs 4 and 5).

Figure 10 shows the same cell model results but the curves for the phenomenological response use $q_1 = 1.25$ and $q_2 = 1.0$. Thus, a very good fit to the cell model results is given by a value of $q_1 = 1.25$ halfway between the original Gurson (1975, 1977) model and Tvergaard's (1982b) suggestion of 1.5. Also, in Fig. 10 modification (32) is utilized with $f_c = 0.03$ and $f_f = 0.13$ to account for the accelerated void growth accompanying coalescence. The value of f_f is chosen to obtain a good approximation to the void volume fraction vs strain curves at $f > f_c$.

Figures 11–13 show the cell model response and the predictions of the modified Gurson (1975, 1977) model for other values of the strain hardening exponent, N, and of the initial void volume fraction, f_0. In these figures, as in Fig. 10, $q_1 = 1.25$, $q_2 = 1.0$ and $f_f = 0.13$. The value of f_c is taken as 0.03 when $f_0 = 0.0013$, Fig. 11, and as 0.055 when $f_0 = 0.0104$, Figs 12 and 13. The void volume fraction is fixed at $f_0 = 0.0013$ in Figs 10 and 11; $N = 0.1$ in Fig. 10 and $N = 0$ in Fig. 11. In Figs 12 and 13 $f_0 = 0.0104$; $N = 0$ in Fig. 12 and $N = 0.2$ in Fig. 13. Comparison of Figs 11 and 12 illustrates the effects of varying f_0 between 0.0013

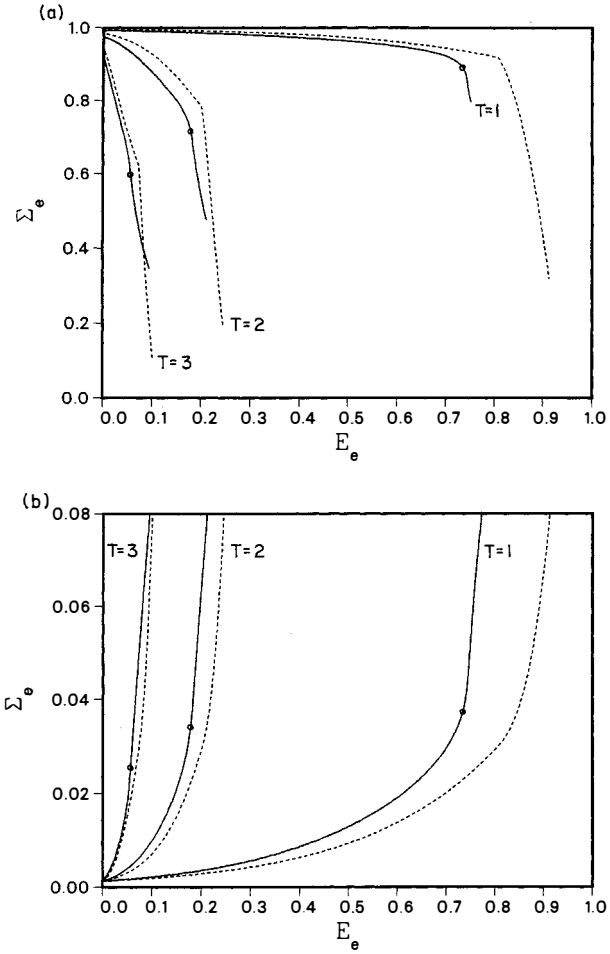

Fig. 11. Comparison of cell model response with the predictions of the modified Gurson (1975, 1977) model using $q_1 = 1.25$, $q_2 = 1.0$ and incorporating the function $f^*(f)$ with $f_c = 0.03$ and $f_f = 0.13$ in eqn (32). Results are shown for $N = 0$, $b_0/R_0 = 1.0$, $f_0 = 0.0013$, with stress triaxialities, $T = 1.0$, 2.0, and 3.0. (a) Macroscopic effective stress vs macroscopic effective strain. (b) Void volume fraction vs macroscopic effective strain. The cell model response is the solid line and ○ marks the shift to a uniaxial straining deformation mode.

and 0.0104 at fixed $N = 0$. In Fig. 12, with $T = 3.0$, the shift to a uniaxial straining state occurs at a void volume fraction significantly below 0.055, but for a non-hardening solid at this high triaxiality, there is little change either in the stress–strain response or the void volume fraction–strain response associated with the shift to an overall uniaxial straining mode.

5. DISCUSSION

The form of eqn (31) was arrived at by Gurson (1975, 1977) through an approximate rigid–plastic limit analysis of a thick walled spherical shell. However, the three conditions, (i) that the flow potential reduce to the isotropic Mises expression for $f = 0$, (ii) that the dependence on void volume fraction is linear when $\sigma_h = 0$, as in pure shear and (iii) that the dependence on stress triaxiality, $\sigma_h/\bar{\sigma}$, be exponential as suggested by the McClintock (1968) and Rice and Tracey (1969) solutions, essentially lead to eqn (31) with Tvergaard's (1981, 1982b) q parameters being arbitrary constants associated with the latter two conditions. Here, axisymmetric cell model solutions that account for void interaction effects and for void shape changes (Fig. 7), are compared with the aggregate stress–strain and the void volume fraction evolution predictions of the modified Gurson (1975, 1977) constitutive relation for proportional stressing histories.

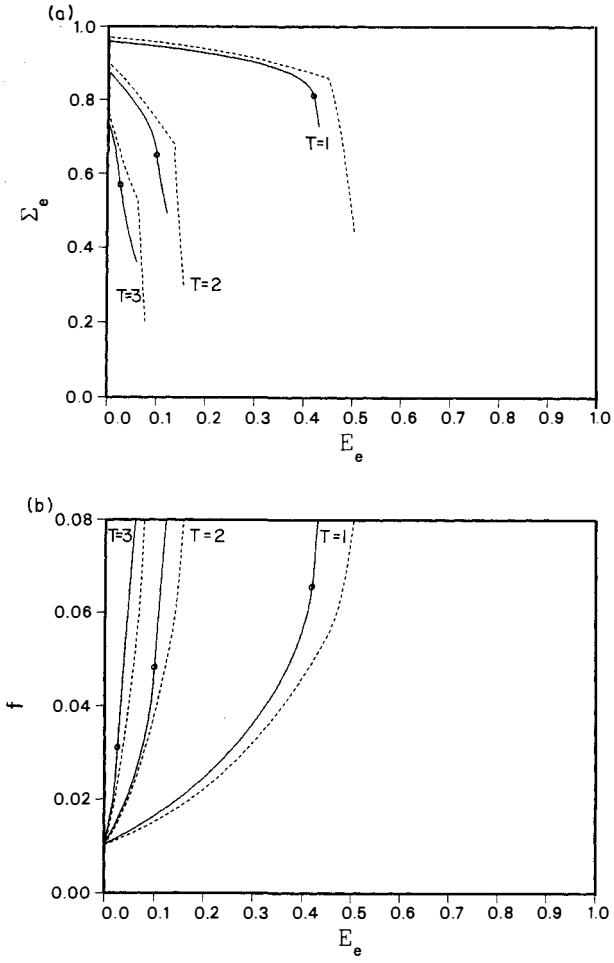

Fig. 12. Comparison of cell model response with the predictions of the modified Gurson (1975, 1977) model using $q_1 = 1.25$, $q_2 = 1.0$ and incorporating the function $f^*(f)$ with $f_c = 0.055$ and $f_f = 0.13$ in eqn (32). Results are shown for $N = 0$, $b_0/R_0 = 1.0$, $f_0 = 0.0104$, with stress triaxialities, $T = 1.0$, 2.0, and 3.0. (a) Macroscopic effective stress vs macroscopic effective strain. (b) Void volume fraction vs macroscopic effective strain. The cell model response is the solid line and ○ marks the shift to a uniaxial straining deformation mode.

Rather good agreement is achieved between the cell model calculations and the predictions of Gurson's (1975, 1977) constitutive relation using the values $q_1 = 1.25$ and $q_2 = 1.0$ for Tvergaard's (1981, 1982b) parameters. Tvergaard's (1981, 1982b) suggestion of $q_1 = 1.5$ was based on a comparison of the cell model and Gurson (1975, 1977) theory results for bifurcation. In Tvergaard (1982b), Figs 4(a), 6(a), 7(a), 9(a), the cell model values for the maximum traction and for the strain at maximum traction generally fall between the $q_1 = 1.0$ and 1.5 results. Becker *et al.* (1988) have used the present finite element cell model formulation but with an experimentally determined matrix uniaxial stress–strain curve and found good agreement between the cell model response and Gurson's (1975, 1977) constitutive relation predictions for $q_1 = 1.25$, $q_2 = 0.95$. Also, Mear (1986) used a spherical shell model to account for void interaction effects, restricted attention to small strains, considered non-proportional loading response, and typically found behavior in line with q values between $q_1 = 1.0$ and 1.5. Hence, with Tvergaard's (1981, 1982b) q parameters taken as $q_1 \approx 1.25$ and $q_2 \approx 1.0$, the cell model and Gurson's (1975, 1977) constitutive relation predictions for aggregate stiffness and porosity are in reasonable accord in a rather wide range of circumstances. However, Figs 10–13 exhibit a systematic trend indicating increasing q_1 values with decreasing strain hardening.

Tvergaard (1982b) analyzed bifurcations from the cylindrically symmetric mode into a localized band type mode, which occurs somewhat after the maximum load (force/unit

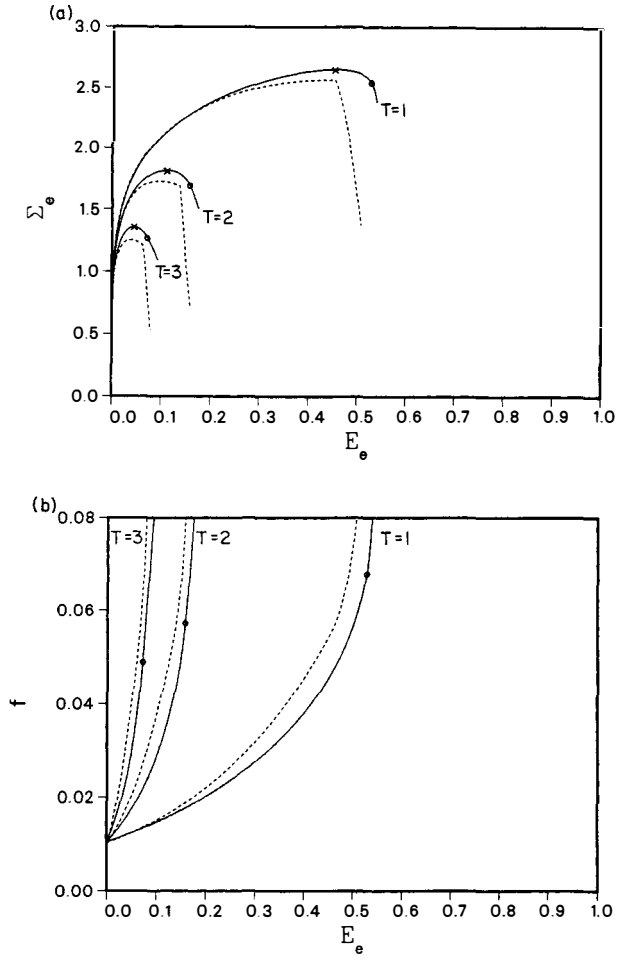

Fig. 13. Comparison of cell model response with the predictions of the modified Gurson (1975, 1977) model using $q_1 = 1.25$, $q_2 = 1.0$ and incorporating the function $f^*(f)$ with $f_c = 0.055$ and $f_f = 0.13$ in eqn (32). Results are shown for $N = 0.2, b_0/R_0 = 1.0, f_0 = 0.0104$, with stress triaxialities, $T = 1.0$, 2.0 and 3.0. (a) Macroscopic effective stress vs macroscopic effective strain. (b) Void volume fraction vs macroscopic effective strain. The cell model response is the solid line and O marks the shift to a uniaxial straining deformation mode.

original area) point. In our calculations, the overall response of the cell model for the void–matrix aggregate exhibits a rather abrupt shift in strain state to a uniaxial straining mode, while maintaining the circular cylindrical symmetry. In this uniaxial straining mode the void grows rapidly with very little increase in overall straining. The calculations here show that even when a localization of the type considered by Tvergaard (1982b) is precluded, straining does localize onto the ligament between neighboring voids.

The value of f_c, which signifies the onset of coalescence in the modification of Tvergaard and Needleman (1984), appears to vary slowly with stress triaxiality and matrix strain hardening, but to depend strongly on the initial void volume fraction. Thus, taking f_c to depend on initial void volume fraction but not on matrix hardening or stress triaxiality is a reasonable approximation over the range of conditions considered here. The appropriate values of f_c for the void volume fractions considered here, $f_0 = 0.0013$ and 0.0104, are 0.03 and 0.055, respectively. Consistent with the present results, Becker *et al.* (1988) found $f_c = 0.12$, 0.06, and 0.04 for initial void volume fractions of 0.07, 0.026, and 0.004, respectively. For the smaller initial void volume fractions ($f_0 \leqslant 0.026$), these values of f_c are significantly lower than the value $f_c = 0.15$ suggested by Tvergaard and Needleman (1984).

The above values of f_c are based on analyses of cells for which $b_0/R_0 = 1.0$ in Fig. 1. As shown in Fig. 8, the attainment of a maximum stress and the shift to a uniaxial straining mode are sensitive to the uniformity of the void distribution. This is consistent with

Tvergaard's (1982b) results for the dependence of the maximum load on cell aspect ratio. However, the initial stress–strain response, at least for low void volume fractions, is well approximated as being a function of void volume fraction, independent of the cell aspect ratio. The effect of the nonuniformity of void volume fraction distributions on localization in a small material element has been investigated by Becker (1987). Using distributions obtained from measurements on sintered iron tensile specimens and characterizing the aggregate in terms of Gurson's (1975, 1977) constitutive relation, Becker (1987) found little influence of the nonuniformity of the distribution on the stress–strain response, but a rather large effect of distribution on the strain to failure initiation.

The focus here has been on the relationship between predictions of Gurson's (1975, 1977) constitutive relation and cell model analyses that account for void interaction effects and for void shape changes. A separate issue concerns the agreement between such analyses and experiment. In their theoretical and experimental study of porous iron notched tensile bars, Becker *et al.* (1988) found that the theoretical predictions provided a good description of porosity evolution and of the strength reduction due to void growth. However, when the stress triaxiality is low, the modified Gurson (1975, 1977) constitutive relation with $q_1 = 1.25$ and $q_2 = 0.95$ underestimates the rate at which the strength decreases with increasing initial porosity and accordingly so do cell model calculations.

Acknowledgements—The support of the National Science Foundation (Solid Mechanics Program) through grant MSM86-18007 is gratefully acknowledged. J.K. is also grateful for the support provided by a National Science Foundation Graduate Fellowship. The computations were carried out at the John von Neumann Center for Scientific Computing. We are pleased to acknowledge helpful discussions with Dr R. Becker of Alcoa.

REFERENCES

Andersson, H. (1977). Analysis of a model for void growth and coalescence ahead of a moving crack tip. *J. Mech. Phys. Solids* **25,** 217.

Beachem, C. D. (1963). An electron fractographic study of the influence of plastic strain conditions upon ductile rupture processes in metals. *Trans. ASM* **56,** 318.

Becker, R. (1983). Finite element modeling of void growth at sulfide inclusions in plane strain tension. M.S. Thesis, University of Pittsburgh.

Becker, R. (1987). The effect of porosity distribution on failure. *J. Mech. Phys. Solids* **35,** 577.

Becker, R. and Needleman, A. (1986). Effect of yield surface curvature on necking and failure in porous plastic solids. *J. Appl. Mech.* **53,** 491.

Becker, R., Needleman, A., Richmond, O. and Tvergaard, V. (1988). Void growth and failure in notched bars. *J. Mech. Phys. Solids*, in press.

Bourcier, R. J., Koss, D. A., Smelser, R. E. and Richmond, O. (1986). The influence of porosity on the deformation and fracture of alloys. *Acta Metall.* **34**, 2443.

Brown, L. M. and Embury, J. D. (1973). The initiation and growth of voids at second phase particles. In *Proc. 3rd Int. Conf. on Strength of Metals and Alloys*, Institute of Metals, London, p. 164.

Budiansky, B., Hutchinson, J. W. and Slutsky, S. (1982). Void growth and collapse in viscous solids. In *Mechanics of Solids* (Edited by H. G. Hopkins and M. J. Sewell), p. 13. Pergamon Press, Oxford.

Goods, S. H. and Brown, L. M. (1979). The nucleation of cavities by plastic deformation. *Acta Metall.* **27,** 1.

Gurland, J. and Plateau, J. (1963). The mechanism of ductile rupture of metals containing inclusions. *Trans. ASM* **56,** 442.

Gurson, A. L. (1975). Plastic flow and fracture behavior of ductile materials incorporating void nucleation, growth and interaction. Ph.D. Thesis, Brown University.

Gurson, A. L. (1977). Continuum theory of ductile rupture by void nucleation and growth: Part I. Yield criteria and flow rules for porous ductile media. *J. Engng Mater. Technol.* **99,** 2.

Mear, M. E. (1986). The plastic yielding of porous metals. Ph.D. Thesis, Harvard University.

McClintock, F. A. (1968). A criterion for ductile fracture by the growth of holes. *J. Appl. Mech.* **35,** 363.

McMeeking, R. M. (1977). Finite deformation analysis of crack-tip opening in elastic–plastic materials and implications for fracture. *J. Mech. Phys. Solids.* **25**, 357.

Needleman, A. (1972). Void growth in an elastic–plastic medium. *J. Appl. Mech.* **39,** 964.

Needleman, A. (1982). Finite elements for finite strain plasticity problems. In *Plasticity of Metals at Finite Strain: Theory, Computation, and Experiment* (Edited by E. H. Lee and R. L. Mallet), p. 387. Stanford University Press, Stanford, California.

Needleman, A. and Rice, J. R. (1978). Limits to ductility set by plastic flow localization. In *Mechanics of Sheet Metal Forming* (Edited by D. P. Koistinen and N. M. Wang), p. 237. Plenum Press, New York.

Needleman, A. and Tvergaard, V. (1984). An analysis of ductile rupture in notched bars. *J. Mech. Phys. Solids* **32,** 461.

Nemat-Nasser, S. and Taya, M. (1976). Model studies of ductile fracture—I. Formulation. *J. Franklin Inst.* **302**, 463.

Nemat-Nasser, S. and Taya, M. (1977). Model studies of ductile fracture—II. Further numerical formulations. In *Finite Elements in Nonlinear Mechanics* (Edited by P. G. Bergan, P. Kr. Larsen, H. Pettersson, A. Samvelsson, T. Søreide and N.-E. Wiberg), p. 211. Tapir, Trondheim.

Pan, J., Saje, M. and Needleman, A. (1983). Localization of deformation in rate sensitive porous plastic solids. *Int. J. Fracture* **21**, 261.
Peirce, D., Shih, C. F. and Needleman, A. (1984). A tangent modulus method for rate dependent solids. *Comput. Struct.* **18**, 875.
Puttick, K. E. (1959). Ductile fracture in metals. *Phil. Mag.* **4**, 964.
Rice, J. R. and Tracey, D. M. (1969). On the ductile enlargement of voids in triaxial stress fields. *J. Mech. Phys. Solids* **17,** 201.
Rogers, H. C. (1960). The tensile fracture of ductile metals. *Trans. Metall. Soc. AIME* **218,** 498.
Saje, M., Pan, J. and Needleman, A. (1982). Void nucleation effects on shear localization in porous plastic solids. *Int. J. Fracture* **19**, 163.
Tvergaard, V. (1976). Effect of thickness inhomogeneities in internally pressurized elastic–plastic spherical shells. *J. Mech. Phys. Solids* **24,** 291.
Tvergaard, V. (1981). Influence of voids on shear band instabilities under plane strain conditions. *Int. J. Fracture* **17**, 389.
Tvergaard, V. (1982a). Material failure by void coalescence in localized shear bands. *Int. J. Solids Structures* **18,** 659.
Tvergaard, V. (1982b). On localization in ductile materials containing spherical voids. *Int. J. Fracture* **18,** 237.
Tvergaard, V. and Needleman, A. (1984). Analysis of cup–cone fracture in a round tensile bar. *Acta Metall.* **32**, 157.
Yamamoto, H. (1978). Conditions for shear localization in the ductile fracture of void-containing materials. *Int. J. Fracture* **14**, 347.